Determining Mid-Ocean Ridge Geography from Upper Mantle Temperature

Xiyuan Bao[1], Tushar Mittal[2], and Carolina Lithgow-Bertelloni[1]

[1]University of California, Los Angeles
[2]Pennsylvania State University

September 22, 2023

Highlights

Determining Mid-Ocean Ridge Geography from Upper Mantle Temperature

Xiyuan Bao, Tushar Mittal, Carolina R. Lithgow-Bertelloni

- Mantle temperatures beneath global mid-ocean ridges exhibit basin-wide differences
- We use machine learning to predict the geographic location of ridge segments based on the sub-ridge upper mantle temperature
- The integrated history of convection and tectonics is recorded in the large-scale patterns observed at mid-ocean ridges

Determining Mid-Ocean Ridge Geography from Upper Mantle Temperature

Xiyuan Bao[a,*], Tushar Mittal[b], Carolina R. Lithgow-Bertelloni[a]

[a]*Department of Earth, Planetary, and Space Sciences, University of California Los Angeles, Los Angeles, CA, USA*
[b]*Department of Geosciences, Pennsylvania State University, University Park, PA, USA*

Abstract

In this study, we examine the influence of the mantle and large-scale tectonics on the global mid-ocean ridge (MOR) system. Using solely seismically-inferred upper mantle temperatures below the melting zone (260-600 km) and an interpretable machine learning model (Random Forest and Principal Component Analysis), we predict, with up to 90% accuracy, the ocean basin of origin of all ridge segments without any prior geographic information. Two features provide >50% of the discriminative power: the temperature difference between the mid-layer (340-500 km) and other depths, and the depth-averaged temperature of the upper mantle. Our result implies that the large-scale geophysical and geochemical differences observed along the MOR system are reflective, not primarily of shallow processes associated with melting, but of long-term tectonic and convective processes in the mantle that determine the present-day upper mantle temperature structure.

Keywords: Mid-ocean Ridge, Potential Temperature, Mantle Convection, Random Forest

*Corresponding author
Email address: `xiyuanbao@g.ucla.edu` (Xiyuan Bao)

2020 MSC: 86-00

1. Introduction

The 60,000 km-long chain of mid-ocean ridges (MOR) is the most visible surface manifestation of plate tectonics and mantle flow. Deep ($>$250 km depth) mantle material is fed to ridges by largely passive convective currents, resulting in decompression melting at depths $<$ 150 km, and the generation of new oceanic lithospheric plates. The plate tectonic factory is hence directly connected not only to the present-day structure of the mantle under ridges but also to the integrated convective and tectonic history of each ocean basin. Consider that, since the breakup of Pangea, the circum-Pacific subduction girdle has produced an influx of cold downwelling slabs towards the mantle beneath the Atlantic and Indian Ocean basins, and a relative absence in the Pacific basin (Supplementary Movie S1, Müller et al., 2019). The downgoing slabs cool the mantle, and the downwelling flow generates a passive return upwelling flow at ridges. Thus, integrated over the last few hundred million years the convective and tectonic history will determine the average temperature of the upper mantle today (e.g., Conrad et al., 2013). We may hypothesize that these tectonic and convective histories may be reflected in the geophysical and geochemical characteristics of the ridge systems of individual ocean basins. For instance, the Pacific ridges have a systematically deeper depth and higher spreading rate (Fig. 1a, b) than the mid-Atlantic ridge system with the Indian Ocean ridge segments having intermediate values (e.g., Gale et al., 2014). Similar differences exist in the major element composition of mid-ocean ridge basalts (MORBs, Gale et al. (2014)).

Previous work on the origin of these basin-scale geochemical and geophysical differences has focused on the correlation amongst spreading rate, ridge depth, and MORB major and trace element chemistry (e.g. Klein and Langmuir, 1987; Brandl et al., 2013; Gale et al., 2014; Niu, 2016), inferences on the mantle temperature (Klein and Langmuir, 1987; Brown Krein et al., 2021), composition of the mantle source region (Niu and O'Hara, 2008), and melt-rock interaction during magma transport (Kimura and Sano, 2012). The premise of these studies is that the degree of partial melting and the nature of melt transport in the melting column is the primary control on the observed variability. However from a geodynamics perspective, we suggest that the differences in ridge characteristics at the ocean basin scale are a consequence not only of shallow melting but of deep mantle structure reflective of convective and tectonic history. Focusing only on shallow processes obscures the large-scale integrative role of mantle convection and tectonic history in shaping the source of mantle melting at the ridge on multiple spatio-temporal scales. However, it is very challenging to analyze the critical role of deep processes from existing studies since the inferences regarding MORB geochemistry and mantle source potential temperature (T_{P}) are strongly affected by the poorly constrained details of the melting process at shallow depths (Stracke, 2021), such as the extent of melt channelization (Spiegelman and Kelemen, 2003; Keller et al., 2017; Brown Krein et al., 2021). For instance, current petrological estimates of the ridge potential temperature (T_{P}) disagree both in absolute value and inferred spatial patterns. Brandl et al. (2013) and Dalton et al. (2014) see a hotter Pacific compared to the Atlantic and Indian Ocean basins, while Brown Krein et al. (2021) see no distinct hemispheric difference. In this study, we take an alternate, data-driven approach to search for unique fingerprints of the ridge system's deep upper mantle (260 - 600 km depth) temperature structure. These variations would serve as inputs for the shallow melting processes that eventually give rise to the observed geochemical variations in MORB lavas.

Our work builds upon earlier attempts to understand the deep mantle contribution to the global ridge system. Early studies, e.g., Ray and Anderson (1994) explored the connection between mantle seismic velocity and ridges, as shear wave speeds are particularly sensitive to temperature. However, Ray and Anderson (1994) were limited by the resolution of the global tomography and sparse mineral physics data and thermodynamic modeling available at the time. They could not infer temperatures directly from the seismic velocities. Dalton et al. (2014) provided a big step forward by using thermodynamic models of the physical properties of mantle rocks to infer mantle temperature at 300 km depth below the ridges from global seismic tomography. They found Pacific ridges to be hotter than those in the Indian and Atlantic oceans. Rowley et al. (2016) also found a possible contribution from active, hotter mantle upwellings to the faster-spreading rates at the East Pacific Rise. While these studies provide important clues regarding the role of convective and tectonic processes on seafloor spreading and MORB geochemistry, they lack predictive power (uniqueness of the mantle fingerprint) or a direct connection to convective and tectonic processes.

In this study, we construct such a predictive model for the basin in which ridge segments are located, starting from the temperature of the upper mantle inferred from a full waveform seismic tomography model and self-consistent thermodynamics (Bao et al., 2022), combined with the power of an interpretable model of classification – the random forest (RF) algorithm (Breiman, 2001). Full waveform seismic tomography models from the past decade (e.g., French and Romanowicz, 2014) provide a more robust and faithful estimate of the amplitude of seismic anomalies, which is crucial for inferences of temperatures. Our work focuses on addressing the following question: Is it possible to use the temperature of the entire upper mantle below the melting zone to classify *a priori* and accurately the oceanic basin ridge segments are located? When we ignore the depth-dependent information, the significant overlap in mantle potential temperatures across basins despite the higher average Pacific temperature (Fig. 1c, using results from Bao et al. (2022), see section 2.2) suggests that the answer to our primary question is not immediately obvious. We answer this question by using the predictive model to test whether the ocean basin individual MOR segments are located can be predicted using only the seismically inferred upper mantle T_{P} without any prior geographical information. While this question may seem superfluous for the present-day, given that we already have the geographical data for each ridge segment, it helps us identify unique sub-ridge mantle temperature patterns associated with each basin and even sub-basin-scale ridge systems. These patterns may be further analyzed with respect to the tectonic and convective history and aid our understanding of whether the variations in the ridge system originate primarily from the deep mantle or shallow processes. In addition, they might provide a framework with which to understand and infer the past temperature of the mantle, enriching tectonic reconstructions. Overall, our 'predictive' evaluation helps towards addressing a fundamental geodynamics question: What is the dominant reason for the differences in ridge properties at the ocean basin scale - shallow melting or deep mantle processes?

Thematically, our work is a counterpart to the recent study by Stracke et al. (2022), who used non-linear dimension reduction and clustering analysis on multiple isotopic data for global MORBs and Ocean Island Basalts. They showed that ridges and hotspots potentially sample distinct sub-basin-scale isotopic heterogeneities, thus highlighting the role of deep mantle processes in controlling ridge composition. Section 2 describes the datasets and analysis methods we use in this study, followed by the results of the random forest analysis in Section 3. Section 4 uses these results to discuss the main implications of our results in the context of the importance of shallow vs. deep mantle processes for ridges.

2. Materials and Methods

2.1. Ridge Database

To test our hypothesis that the unique sub-ridge temperature features exist, we start by sampling mantle properties underlying MOR segments in the three major ocean basins (Pacific, Atlantic, Indian). We use the segment definitions from Gale et al. (2014) database with some filtering (choosing 655 out of 711 segments) to a) avoid more complex tectonic settings (back-arc basins and ultra-slow ridges) and b) simplify classification. The Gale et al. (2014) ridge segments are determined based on along-ridge axial depth variations, ridge offsets, transform faults, and non-transform offsets. Using these segments is a reasonable choice for our question of interest rather than a uniform sampling per km of the ridge since each segment would correspond to a unique tectonic/convective regime. Although our primary focus is on inter-basin variations, we also test the robustness of our conclusions by doing ridge-basin classification for the entire database (including smaller basins in the Arctic, Caribbean, and Red Sea), as well as finer sub-basin ridge system classification (discussed in section 3.2).

2.2. Temperature Inference

Following Bao et al. (2022), we extract shear wave seismic velocity from tomographic model SEMCUB-WM1 (French and Romanowicz, 2014) and convert it to temperature. We validate our results with 4 additional global tomographic models (Ritsema et al., 2011; Simmons et al., 2010; Schaeffer and Lebedev, 2013; Debayle et al., 2016). We extract velocity anomalies directly beneath each ridge segment, without any lateral averaging, from 260 to 600 km depth in 20 km intervals. This depth interval allows us to capture sufficient information given the radial spline basis functions used in recent global tomography models (e.g., French and Romanowicz, 2014). We focus on depths below 260 km to avoid the strongly attenuated seismic velocities, potentially caused by partial melt. Dry melting starts $<\sim$ 100 km depth beneath the ridge and at $<\sim$ 200 km in the presence of volatiles (Keller et al., 2017 and references therein). A depth $>$ 260 km is sufficient to avoid even the melting-influenced regions of intraplate volcanism, as seen seismically (Debayle et al., 2020) and geochemically (Ball et al., 2021). Because the velocity to temperature conversion is non-linear (Bao et al., 2022), we convert the shear-wave velocity anomalies to temperature using HeFESTo (Stixrude and Lithgow-Bertelloni, 2005, 2011). HeFESTo is a self-consistent thermodynamic model of the equilibrium phase assemblage of mantle minerals and their physical properties at a given pressure, temperature, and fixed bulk composition. We use the conservative premise that the upper mantle is compositionally homogeneous, consisting of Depleted MORB Mantle (DMM, Workman and Hart, 2005) and any differences in seismic properties are thermal in nature (Dalton et al., 2014). Because the mantle is thermally heterogeneous due to multi-scale flow, potential temperature is expected to be depth-dependent, consistent with our estimates. Our final temperature data for the ridge segment catalog is high-dimensional (18 depth layers per ridge segment, Fig. 2), which demands a strategy for dimensional reduction discussed below (section 2.3).

2.3. Data Processing and Classification

We first use a linear classifier, i.e., multinomial logistic regression, to predict the basin where each ridge segment is located based on the MOR mantle temperature profiles (260 to 600 km depth, one per ridge segment). Specifically, we try to find lines in the space of each input pair (e.g., between temperature at 2 depths) to separate out the different basins. A softmax function (Bridle, 1989) is used to find the maximum probability of the particular class and to give a prediction. However, this yields low accuracy irrespective of whether we use dimensionality reduction (60% accuracy) or not (65% accuracy). This suggests that there is no clear, linear predictive separation between each ocean basin ridge segments (e.g., Fig. 3). The high-dimensional nature of the raw data (i.e., 18 depth layers) also makes the problem challenging. Thus, we need a higher-order machine learning model that can handle both linear and highly nonlinear relationships and remain interpretable. We further desire that the model features be physically meaningful quantities that can be related to dynamical processes, such as the average temperature of the upper mantle (related to long-term plate organization, e.g., Gurnis, 1988), and the difference in temperature between layers which can be linked to various convective length scales.

Dimensional reduction using Principal Component Analysis (PCA, Jolliffe, 2002) satisfies the requirements set above for optimal, interpretable classification. PCA is a commonly used method for high-dimensional datasets and calculates orthogonal principal components (PCs, Fig. 4). Each PC is a linear combination and weighted sum of the normalized T_{P} at the 18 distinct depths under each ridge segment. That is, $PC^i = \sum W_d^i \hat{T}_{p_d}$, $\hat{T}_{p_d} = (T_{p_d} - \mu_d)/\sigma_d$, where W_d^i is the weight for ith PC at depth d; $\hat{T}_{p_d}$ and T_{p_d} are the normalized and original potential temperature at depth d, respectively; μ_d and σ_d are the average potential temperature and standard deviation for all ridge segments at depth d, respectively. We normalize and rescale the original temperatures (from T_{p_d} to $\hat{T}_{p_d}$) for each depth before using it in the PCA calculation, to have zero mean and unit variance to achieve better performance (Duda et al., 1973). PCs are sorted from large to small values based on how much variance they can represent in the data. PC1 covers the largest variance of the data, PC2 the second largest, and so on for the remaining principal components. Mathematically, PCs are obtained using the eigenvector of the co-variance matrix of the normalized original data, and sorted by the corresponding eigenvalues. Because we have 18 depths, there will be 18 PCs in total. Analyzing the PCs that capture the main variance ($\sim 99\%$) equates to projecting the data to a reduced dimensional space.

Instead of using a covered variance-based cutoff, We determine the optimal number of PCs to be used in our analysis based on their final performance in the subsequent machine-learning model.

Given the poor performance of a linear classifier even with PCs as inputs ($\sim$ 60%), we choose to use a nonlinear supervised classifier like Random Forest (Breiman, 2001) for our primary analysis here. Using the PCs as inputs, we train a Random Forest (RF) model to predict the ocean basin in which ridge segments are located. RF is a robust classification algorithm (reduced sensitivity to overfitting) and generates interpretable decision trees (Fig. 5a). RF consists of a decision tree generation algorithm, which chooses only one feature (i.e., PC) at each node and divides the data into two branches based on a cutoff value. To determine what PCs to use and their cutoff value for each tree branch, the tree algorithm calculates the entropy or Gini impurity G for each possible PC & cutoff combination. At each node, we have $G = \sum_k p_k(1 - p_k)$, where p_k is the proportion of each class (i.e., ocean basin) k. A low entropy or Gini impurity measure indicates that the sub-node/branch would be dominated by one class and it is thus a good choice for dividing the tree. This process is repeated until the whole dataset is classified by a tree consisting of many branches. Overall, the algorithm optimizes the PC selection and cutoffs at each branching point to match the input classification labels (here the ridge basins of origin). For each input datapoint consisting of a set of PC values, the final classification is the value of each end node (leaf node) that the datapoint reaches after traversing the trained tree model (e.g., Fig. 5b). A key feature of the tree-based classification algorithms is that they make it easier to understand the classification and the importance of each input feature in the final predictive classification model. RF generates a series of decision trees (here N = 20) as a forest and takes the predicted probability of the segment in a certain basin averaged from each tree. There are two built-in levels of randomness to avoid overfitting: 1) Random resampling of the dataset via bootstrapping when training each tree, and 2) PC selection from a randomly selected subset of PCs when growing the tree.

The nonlinear nature of the algorithm and its randomness enable RF to handle the complicated ridge database robustly. To further avoid overfitting and improve the robustness of the prediction, we also randomly split the input PC data into training (80%) and testing (20%) sets. We repeat this 50 times to calculate the average classification accuracy. The modeling pipeline is constructed using Orange which enables visual programming for data mining (Demšar et al., 2013). Note that with PC as input of Random Forest, our model is similar to the Rotational Forest. In Rotational Forest, the raw feature is split into subsets randomly, and then PCA is performed for each subset. The result is then used as input for the RF algorithm (Rodriguez et al., 2006).

When we visualize data in PC pair space (or input temperature variable space) with scatter plots in Orange (Demšar et al., 2013), it can compute the most informative projections. For each point, Orange finds 10 nearest neighbors in the projected 2-D space, e.g., two PCs. It then checks the number of points out of 10, with the same ocean basin. The averaged number across the neighborhood of all points gives the final score, and we consider the PC (or temperature) pair with the highest score the most informative projection. In Figure 3, we show the results of this analysis for a pair of input temperature data variables.

3. Results

3.1. Potential Temperature

Figure 2a shows the map of inferred T_{P} averaged over 260-600 km depths. The mean and median T_{P} of the Pacific are the hottest overall, while those of the Indian and Atlantic basins overlap (Fig. 1c), consistent with Dalton et al. (2014). The modal T_{P} for Pacific ridges is similar to that of Indian ridges but slightly hotter than that of Atlantic ridges. Overall, Indian ridges have T_{P} distribution intermediate between Pacific and Atlantic ridges. We see regional in-basin lateral temperature variations similar to Dalton et al. (2014) and Bao et al. (2022). While the map (Fig. 2a) and overall statistics (Fig. 1c) already reveal some differences among basins, we observe additional multi-scale vertical variations, which we discuss in section 4.2 (Fig. 2b).

3.2. Principal Components and Random Forest

We find that the first 5 PCs cover $> 99\%$ of the variance in the temperature data (Fig. 6a). The proportion of variance explained by each PC decreases dramatically from more than 75% for PC1 to less than 1% for PC5. To understand what each PC represents physically, in Fig. 4a, we show the weighting coefficients of the linear combinations of PCs using the weight matrix of the first 5 PCs. For PC1, the weights are ~ 0.2 at all depths. Thus, PC1 corresponds to the scaled average T_{P} over all depths. Other PCs have an average weighting of 0, meaning they emphasize the T_{P} differences at depth for length scales smaller than the whole upper mantle. For example, the weighting coefficients for PC2 decrease from 0.3 to -0.3 from 260 km to 600 km, essentially giving the difference in T_{P} between the upper half of the upper mantle (260-420 km) and the transition zone (440-600 km). The coefficients for PC3 are positive around 400 km (340-500 km) and negative at the top (260-320 km) and bottom (520-600 km); thus PC3 quantifies the contrast between mid-upper mantle depths (340-500 km) and other depths (especially $<$300 km, where the weight is the most negative at about -0.5). Finally, PC4 and PC5 represent variations at smaller length scales ($\leq$80 km). The first 5 PC values for all ridge segments are shown in Fig. 2b.

Choice of PCs: PC1, or essentially the average upper mantle T_{P}, shows substantial overlap across basins around 1300-1500 °C (Fig. 1d), and it is insufficient for accurate basin classification. As PC1 is only the bulk temperature of the upper mantle, information at smaller length scales (through other PCs) is required to distinguish ridges from basins with similar bulk temperature from each other. To have a parsimonious model, we first try to predict the basin geography with just one other PC by finding the most informative 2-D projection, which gives the best classification accuracy among all PC pairs. We find that this is the PC1 vs. PC3 projection shown in Fig. 4b. The Pacific segments lie primarily on the right of the projection (PC1> -4), while the Atlantic can have extreme PC3 values (> 2 or < -2). Although one can approximately predict ocean basins based on this zoning, the PC1 and PC3 in each basin still overlap significantly. Thus, the predictive accuracy is less than 60% and we need more PCs and length scale information. The zoning in Fig. 4b also reinforces the need for non-linear classifiers since the boundary between different ocean basins is curved and complex.

To determine the best number of PCs in the RF model, we add one PC at a time, in the order of descending variance covered (e.g., PC1, PC1+PC2, PC1+PC2+PC3, and so forth), and calculate the classification accuracy as a function of the number of PCs (Fig. 6b). Not surprisingly, classification accuracy generally increases with more PCs. However, the increased accuracy gain generally reduces as the PC index increases. Three PCs are enough to achieve 70% classification accuracy. To reach 80% accuracy, we must include PC1 to PC5 (accuracy = 82%). Since adding more PCs does not significantly improve the accuracy, we will use the first 5 PCs for the subsequent analysis. We get prediction accuracies from 75% (Pacific) to 90% (Atlantic), shown in Table 1 as the confusion matrix.

Trained tree model : A typical example of how PCs work in RF is shown in Fig. 5b, which shows one decision tree of RF. At the root node where we have all samples (a random subset of all ridge segments), RF finds that PC1 can best split the data by bifurcating the samples at PC1 = 4.99 so that the child node with PC1 $>$ 4.99 (node A) is dominated by Pacific ridges. The other child node (node B) with PC1 $\leq$ 4.99 has fewer Pacific samples. In this way, the child nodes are more uniform and the entropy of the child nodes is minimized. Next, a random subset of PC candidates is generated at node A, and RF chooses to use PC4 = -0.22 to further bifurcate node A to A1 and A2. Consequently, the child node A1 has an even higher portion of Pacific segments than node A, while node A2 only has samples from the Atlantic Ocean. Similarly, node B is bifurcated at PC3 = 0.25 to B1 and B2 such that B1 has very few Pacific samples. A similar procedure is applied to A1, B1, and B2 with PC2, PC5, and PC1, respectively, and their child nodes repeatedly until the child node has four samples (or less) or samples in the child node are purely from one basin (like A2). We call these end nodes leaf nodes. Overall, as the decision tree grows from the root node to the leaf nodes, we gradually minimize the entropy at the next level and have one basin dominate each leaf node.

Classification robustness : We find that the classification accuracy is robust for all other tomographic models examined and ranges from >83% (Debayle et al., 2016) to 90% (Ritsema et al., 2011; Simmons et al., 2010; Schaeffer and Lebedev, 2013). This higher accuracy may be because other global tomographic models explored here contain less heterogeneity at shorter wavelengths at depth (e.g., discussion in Meschede and Romanowicz, 2015). Consequently, these models suppress in-basin temperature variation and emphasize inter-basin differences. We also notice the weight matrix is reasonably consistent across models, i.e., PC1 always gives the average while each of the other 4 PCs gives the differences of the same layers. However, the sign of weights in certain PCs may flip (Fig. 7). These results are not unexpected as global tomographic models are broadly consistent with each other in the upper mantle. In addition, we can obtain a slightly improved classification accuracy (from 82 to 86%) if we average the inferred T_{P} in a disc, with radius $R = 500$ km centered at each ridge segment, at each depth. The local average temperature beneath the ridge segment incorporates additional environmental information (i.e., cold and hot anomalies) and suppresses in-basin small-scale lateral variations.

Results with sub-basins : While we focus on the classification of three large main basins, the inclusion of the other small regions like the Arctic, Red Sea, and Caribbean ridge systems only leads to negligible decreases (1%) in classification accuracy. Therefore, our primary conclusions do not change with the full mid-ocean ridge database of 771 segments. We further test our ability to predict smaller tectonic units within ocean basins (sub-basin ridge systems, e.g. East Pacific Rise). To do this, we slightly simplify the groups in the ridge database by merging the Chile Ridge with the Pacific-Antarctic Ridge and the Atlantic-Antarctic Ridge with the Mid-Atlantic Ridge. We then obtain a sub-basin ridge system map based on our classification (Fig. 8) with an acceptable accuracy of 74%. Using the local temperature averaged inside a 500 km-radius disc surrounding each ridge segment, we get 80% accuracy because lateral variations within each ridge system are suppressed.

4. Discussion

Our results show that we can determine the ocean basin of origin with 80 to 90% accuracy. The robustness of our results suggests that the sub-ridge mantle temperature is distinct across basins and could be an excellent indicator of large-scale convective contributions to surface differences in the MOR system. Conceptually, our classification model can be regarded as a non-linear function that takes the present sub-ridge mantle structure as input, decodes the hidden signature of the integrated records of past tectonic and convective history, and converts the signature into location information of the ridges in terms of the basin of origin or smaller tectonic units, such as sub-basin ridge systems. *The hidden signature from the deep mantle is sufficient to provide robust long-wavelength information without introducing* *any shallow or surface observations such as MORB chemistry or spreading rate and ridge depth.*

4.1. Feature importance

The high classification accuracy suggests that the deep thermal structure beneath MOR is distinct enough to discriminate between ocean basins. Each principal component represents the sub-ridge temperature heterogeneity at different length scales, ranging from the entire upper mantle (PC1) to half (PC2) to 1/3 (PC3) of the upper mantle, and even smaller depth intervals (PC4 and PC5). Our results thus reveal the length-scale of thermal and chemical heterogeneity subsisting in the mantle and contributing to the integrated convective record. To assess which features (i.e. PCs) contribute to classification accuracy the most, we use feature importance analysis methods. For non-linear classifiers such as RF, we can use the permutation feature importance method (Breiman, 2001) to compute feature importance. This approach randomly permutates the data of a given PC and computes the corresponding decrease in classification accuracy with respect to the default case (Fig. 5a). We find that PC3 is the most critical feature with >30% importance, while PC1 is the second most important (>20%). Thus, PC3 and PC1 together provide more than half of the discriminative power of the 5 PCs.

4.2. Physical interpretation

4.2.1. PC1

PC1, the average T_{P} over all depths and the second most important feature, broadly represents the current convective vigor of the upper mantle column. The distinct hemispherical pattern (higher PC1 in the Pacific, Fig. 2, 1c) is consistent with previous studies (Brandl et al., 2013; Dalton et al., 2014) and can be linked to past subduction history.

For instance, the Pacific ocean evolved from the Panthalassic ocean. It was filled with in-basin spreading ridges and was also surrounded by an outward subduction girdle predating the formation of Pangea ($\sim$300 Ma). Over that period there was also significant intraplate hotspot volcanism resulting in large oceanic plateaus potentially reflective of the higher basin temperature. In contrast, the Atlantic region developed from the rifting of Pangea $\sim$180 Ma and the formation of the mid-Atlantic ridge system. The Indian Ocean has a more complex tectonic history – it has undergone in-basin subduction, ridge spreading, and the closure of the Tethys (Müller et al., 2019). These different tectonic histories, in particular, the presence or absence of in-basin subduction and the subduction of slabs away from one basin and towards another, can change the first-order thermal structure of the mantle under each basin and is reflected in the MOR temperature today (Fig. 1c).

The observed hemispherical mantle temperature difference between ocean basins may reflect a degree-1 difference from the surface to the core-mantle boundary. It has been suggested that the residual topography and lithospheric thickness seem to also present a similar hemispherical pattern (Stewart et al., 2023), which might be linked to the differences between the corresponding mantle domains (the dashed line in Fig. 9). Such degree-1 difference may be sustained over the last 200 Mys - while subduction was directed away from the Pacific towards the African (Atlantic and Indian) domain, the corresponding mantle domains persistently had a degree-2 convection regime

(Conrad et al., 2013, black arrows in Fig. 9). The persistence of the degree-1 structure as well as the degree-2 flow may be also supported by the possible anchoring of the Large Low Shear Velocity Provinces (LLSVPs) above the core-mantle boundary located under the Pacific and African plates (e.g., Torsvik et al., 2010). Although the origin and specific nature of the LLSVPs are beyond the scope of this discussion, their presence and relation to past subduction likely influenced the thermal structure of the mantle under each ocean basin.

Beyond recent (< 200 My) subduction history, the long-term convective and tectonic history, such as the presence of supercontinents, may also alter the thermal structure of the mantle under each basin (Gurnis, 1988; Jellinek and Lenardic, 2009; O'Neill et al., 2009; Lenardic et al., 2011). Karlsen et al. (2021) argue that Rodinia, a longer-lived (1.1-0.7 Ga) supercontinent, might have allowed more heat to accumulate under the Pacific mantle domain in contrast to the impact of the shorter-lived Pangea (300-180 Ma) on the African domain. The additional supercontinent insulation may be partially responsible for the present-day hemispherical temperature difference T_{P} at depth (Fig.2a), despite faster cooling in the Pacific due to higher spreading rates after the breakup of Pangea (Karlsen et al., 2021).

Besides the impact on basin-wide average temperature and PC1, past subduction may also explain regional low PC1 values. For instance, a coherent slab-like structure has been observed beneath the Southeast Indian Ridge in seismic tomography models (Simmons et al., 2015) with a part of this potential slab remnant still trapped in the transition zone (Gurnis et al., 1998). This subduction event dates back to the Mesozoic and terminated near the edge of East Gondwana $\sim$ 140Ma. The presence of a trapped slab in the transition zone may explain the low temperatures and PC1 value of the associated nearby ridge ($T_{\mathrm{P}} \sim$ 1250 °C, PC1$\sim$ -10, green box in Fig. 2) and contribute to the Indian basin's ridge system intermediate nature. These observations suggest a potentially persistent effect of subduction on upper mantle structure and temperature for over 100 Myr.

4.2.2. PC3

Interpreting PC3 – the difference in temperature between the middle of the mantle (340-500 km) and other depths – is more challenging. PC3 is more distinct basin-wide (Fig. 1f), and consequently, PC3 dominates the classification as indicated by the feature importance. The confusion matrix of our model (Table 1) shows that the smallest portion of mislabeled samples is between the Atlantic and the Indian region (around 8%) which is less than those related to the Pacific (usually >10%). This result illustrates that the hemispherical, first-order differences from PC1 are insufficient to determine whether a ridge segment is inside the Pacific Ocean (Fig. 1d). The modal PC3 value is highest in the Atlantic, then the Indian, and lowest in the Pacific (Fig. 1f). What controls the different temperatures at the length scale of 1/3 of the upper mantle across ocean basins? We posit that PC3 variations are potentially related to mantle flow associated with plume-ridge interaction as well as the interaction of the ridge with large-scale mantle upwellings (e.g., Ribe et al., 1995; Sleep, 2002; Gassmöller et al., 2016; Gibson and Richards, 2018). A detailed analysis of the physical interpretation of PC3 will be discussed in a future companion paper.

4.2.3. PC2, PC4, PC5

PC2, the difference between the transition zone and mantle above the transition zone, is a feature that describes a larger length scale than PC3, and far larger than PC4/PC5. However, its importance is less than 20%, only about half and 80% of that of PC3 and PC1, respectively (Fig. 6c). Interestingly, we find that while PC2 covers ∼15% variance in contrast to 1% or less for PC4 and PC5 (Fig. 6a), the three PCs have similar feature importance (Fig. 6c). We attribute this to the fact that no single dynamical process dominates the difference at the three scales globally. Consequently, we observe no obvious modal/median difference among basins for PC4 and PC5 and PC2. But there are still differences between basins in terms of the shape of the density distribution, especially the distribution edges (Fig. 1e, g, h), so that each of PC2, PC4, and PC5 provides around 15% classification accuracy. A deeper physical understanding of the origin of these variations, such as the potential role of transition zone phase transitions and discontinuity topography, will be the subject of future work. We note it is hard to further improve classification accuracy to near 100% even when including more PCs. This may indicate the role of neglected dynamics such as those related to the melting process or heterogeneities shallower than 260 km depth.

5. Conclusions

With thermodynamically inferred upper mantle temperature and a robust machine learning model, we show that we can predict the ocean basin where ridge segments are located with at least >80% accuracy (Fig. 6b) using only temperature information from the mantle column beneath the ridge below the melting zone. Unlike surface ridge characteristics (depth, geochemical signals, etc.) which can be altered by complex shallow melting processes, upper mantle temperature is a proxy that records 100s Myr of history of plate tectonics and mantle convection (Fig. 9). Our results help reveal the significant contribution of the deep mantle to large-scale MOR geophysical signals and suggest distinct inter-basin and even sub-basin deep mantle variations. The cluster analysis of ridge isotope geochemistry in Stracke et al. (2022) highlighted similar spatial mantle compositional variations. These two results together reinforce the idea that the mantle is recording the integrated tectonic and convective history of the last few hundred million years, leading to inter-basin and sub-basin temperature and isotopic variations. We anticipate that future studies may be able to predict the long-wavelength features of MORs using the mantle temperature alone and analyze the disentangled effect of shallow melting processes on various geophysical, geochemical, and petrological observations at MORs. Such analysis could also be extended in space (other isochrons in the ocean basins) and time (past MOR features) and help understand the fingerprints of past mantle convection processes in present-day mantle temperature heterogeneity or conversely temperature heterogeneity in the past.

6. Data Availability

The machine learning pipeline was constructed using Orange Demšar et al. (2013), available at `https://orangedatamining.com/` licensed under GNU version 3.0 or later. The compiled ridge database, including the seismic velocity and inferred temperature, along with the Orange workflow file, are available at https://figshare.com/s/1cc8a5bc0d6faa469fe1 (DOI:10.6084/m9.figshare.22256035). The thermodynamic package HeFESTo Stixrude and Lithgow-Bertelloni (2005, 2011) is available at https://github.com/stixrude/HeFESToRepository, and the parameter set is available at https://github.com/stixrude/HeFESTo_Parameters_310516. The Movie S1 was created with Gplates portal at http://portal.gplates.org/ Müller et al. (2016).

7. Acknowledgments

This project is supported by the National Science Foundation under grant EAR-1900633 to CLB. CLB was also supported by the Louis B. and Martha B. Sclichter Chair in Geosciences fund. TM was supported by the Crosby Fellowship at MIT.

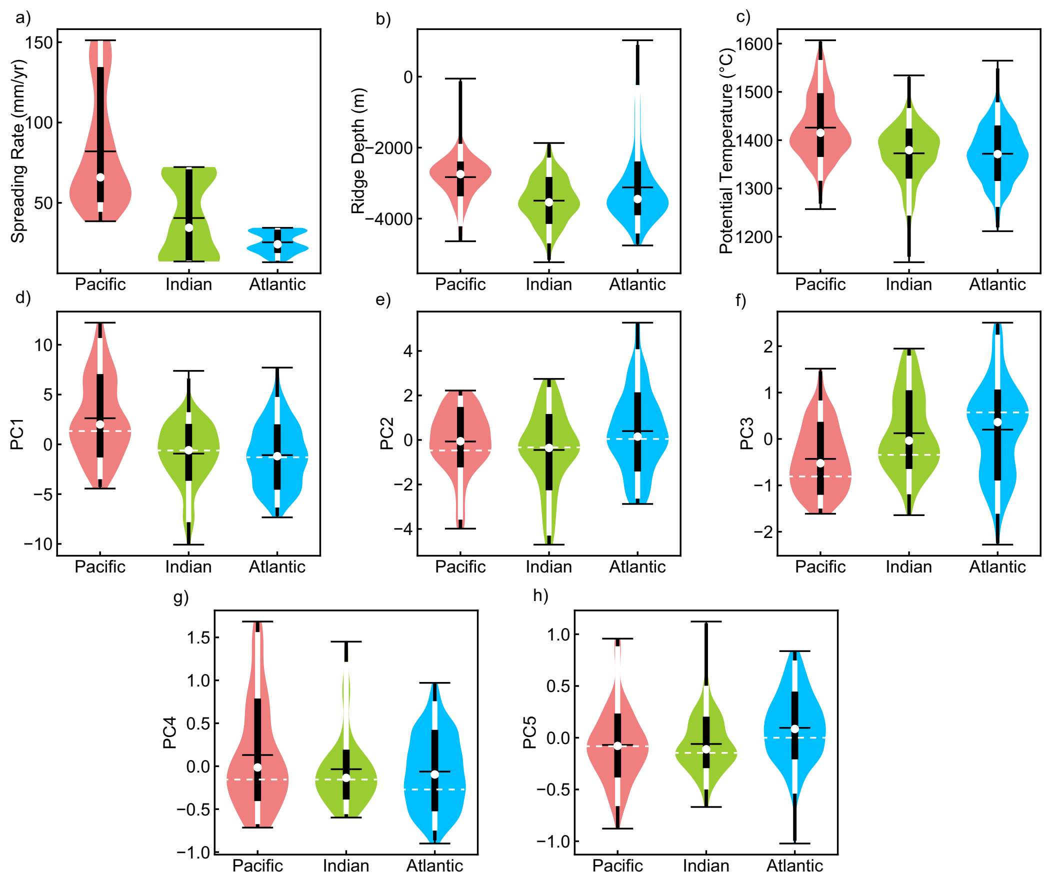

Figure 1: Violin plot of number density distribution of geophysical characteristics of each ocean basin. a) Ridge Depth. b) Spreading rate. c) Potential temperature stacked over all depths. d-h) PC1 to PC5. For each column, the horizontal bars are max, average, and min from top to bottom. The end points of vertical black and white bars are central 99, 95, 68 percentile from the median (white point). PC1 (d) and PC3 (f) have modal value position (dashed line) more distinct in the three basins, while PC2 (e), PC4 (g) and PC5 (h) have indistinguishable modal value positions in the three basins.

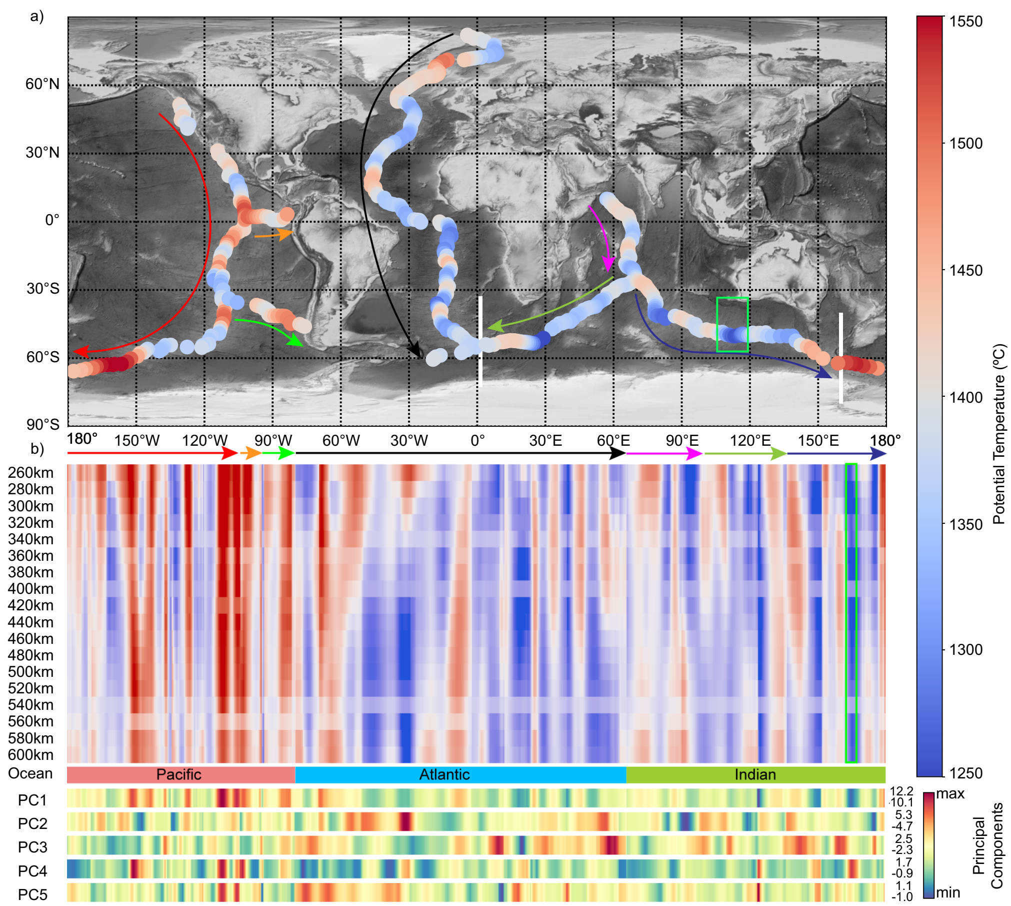

Figure 2: The inferred temperature T_P for MOR segments in the major ocean basins: the Pacific, the Atlantic, and the Indian. a) Map view of T_P averaged over all depths. White lines are ocean basin boundaries. b) T_P at depth. The order of ridge segments is shown with arrows in both panels. The ridge in the green box in both panels are possibly related to an ancient slab (Simmons et al., 2015). The bars on the bottom show the corresponding principal components for each segment.

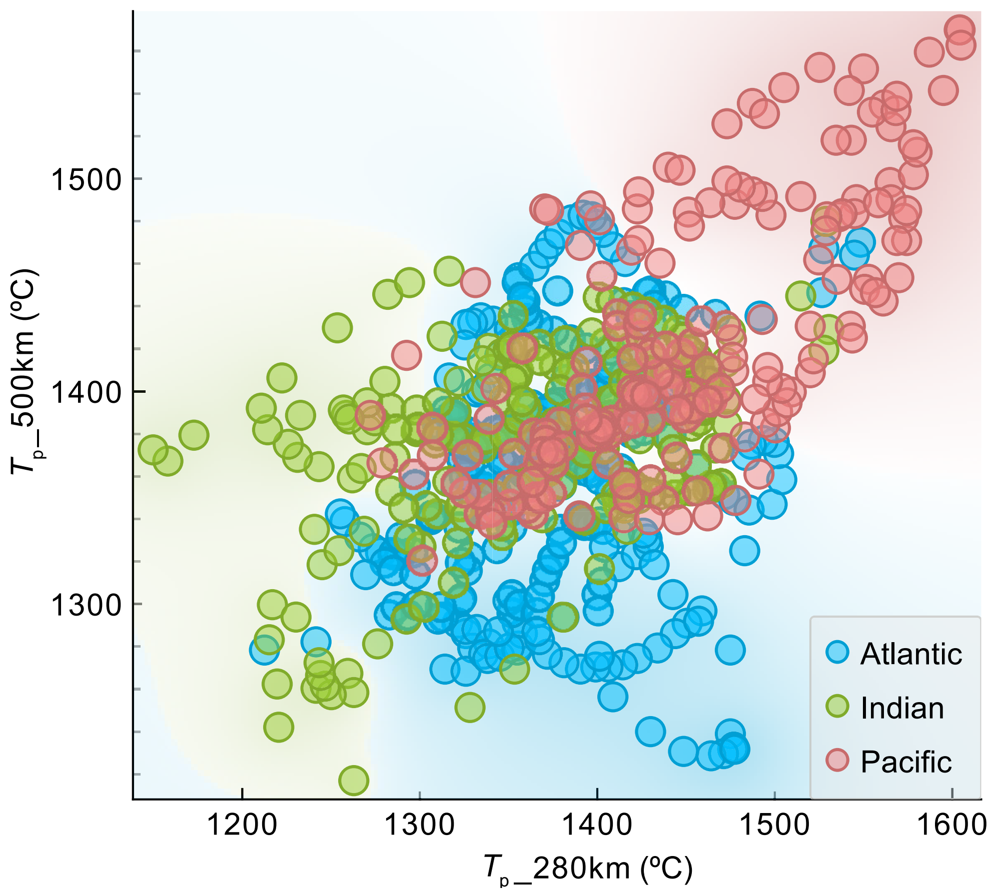

Figure 3: Scatter plot of potential temperature T_P at 280 km versus 500 km. This is the most informative projection among all pairs of temperatures, showing the best basin zoning, shown by the background colors.. Background colors are based on the density of points from each ocean basin in that space. Note that data from different basins are not easily separable with this linear classifier.

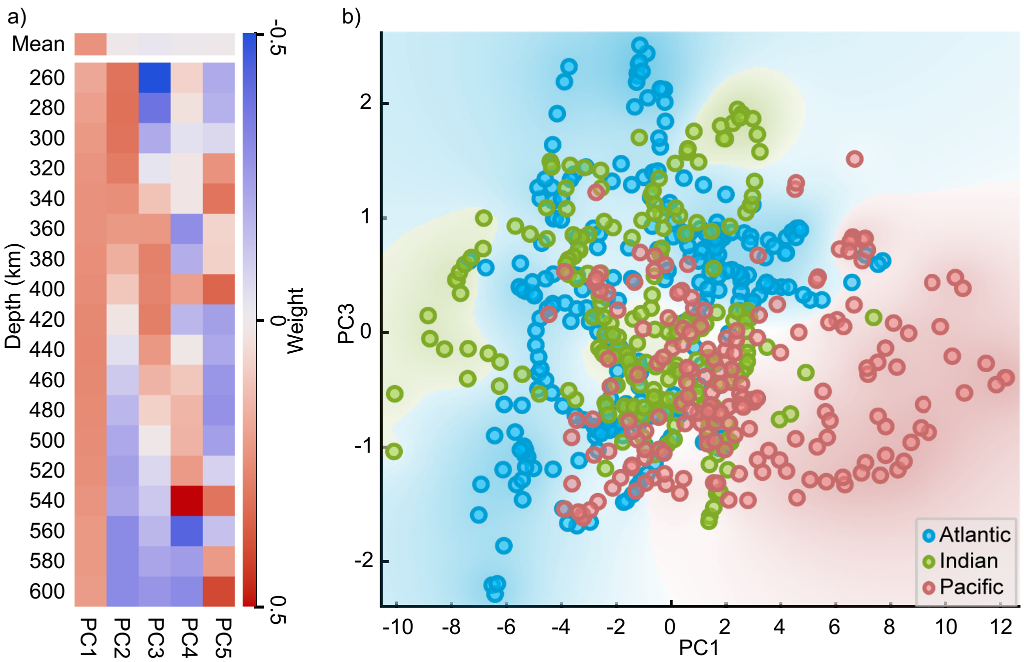

$PC^i = \sum_d W_d^i \hat{T}_{\mathrm{P}d}$ $\quad$ W_d^i: weight for i th PC at depth d

$\hat{T_{\mathrm{P}_d}} = (T_{\mathrm{P}_d} - \mu_d)/(\sigma_d)$ $\quad$ at depth d $\quad$ T_{P_d}: potential temperature μ_d: average σ_d: standard deviation

Figure 4: Principal Component Analysis (PCA). a) Each PC is a weighted sum of normalized T_{P} at depth using the equations shown at the bottom. Individual weights (W_d^i) are shown as a heatmap. The top row shows the average weight of each column (over all depths). b) Ridge segment data is shown in the most informative space PC1 versus PC3 among all PC pairs. Background colors as in Fig. 3

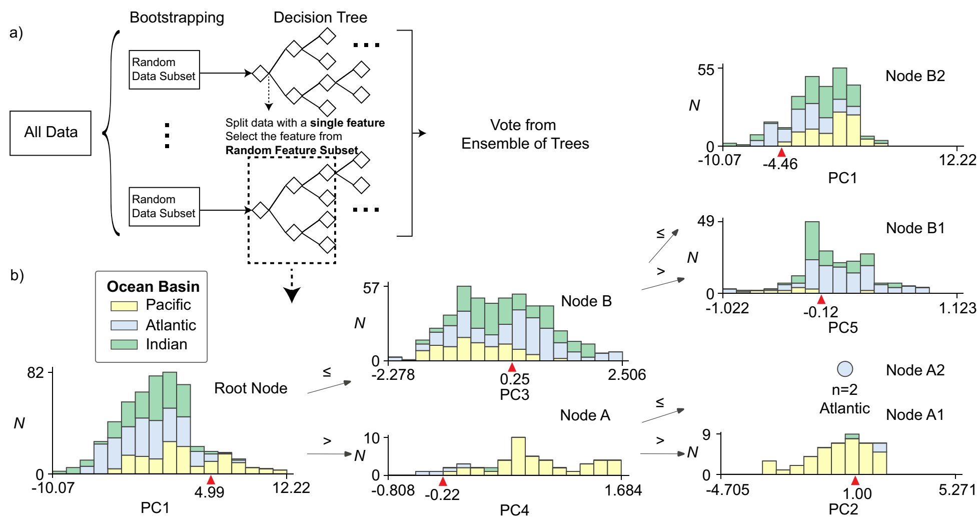

Figure 5: The Random Forest (RF) model. a) Schematic of RF. Data are randomly sampled as subsets with replacement (Boostrapping), and each subset is fed to a different decision tree. In each tree the data are bifurcated multiple times. For every bifurcation, the tree chooses a best PC from a random subset of PCs. Compared with the parent node, the child nodes are purified, i.e., they are gradually dominated by an ocean basin after bifurcation. The end node (leaf node) can predict probability of the ocean basin based on its basin fraction. The ensemble of trees then vote for the classification. b) The top 3 levels of one decision tree in the RF (dashed box in panel a). Each node bifurcates based on the PC shown (x axis) at the point indicated by the red triange. The y axis is the number of data points. The upper child node has data no larger than the point indicated by the red triange in its parent node, and vice versa. The tree stops at leaf nodes like A2, when all the points belong to one basin only, or with no more than 4 data points.

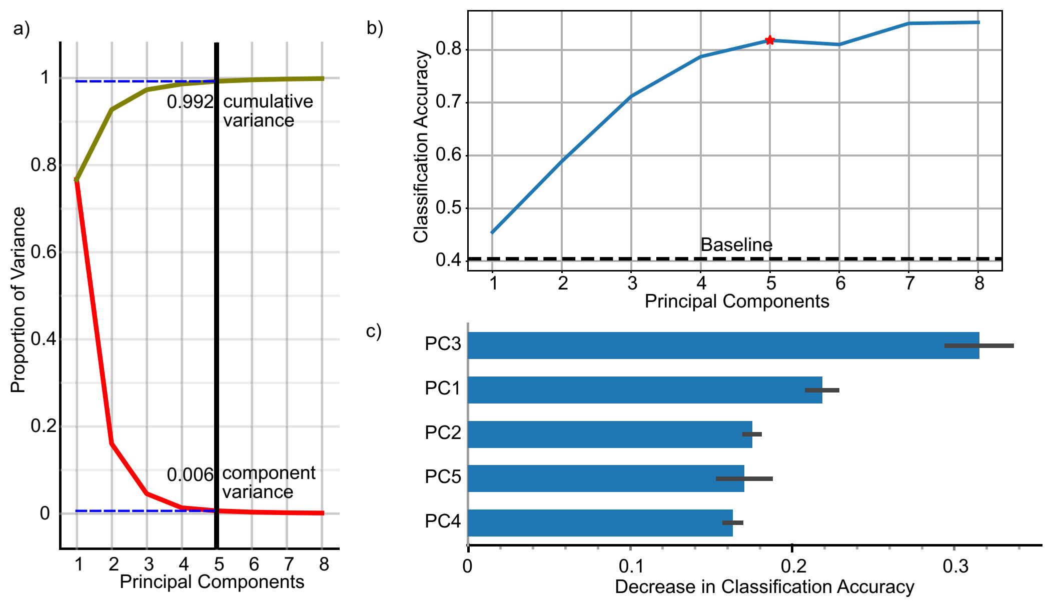

Figure 6: Effect of the first few PCs. a) The proportion of variance covered by each PC (red) and cumulative proportion (dark olive green). b)The cumulative Classification Accuracy with PC1 to PC8. The star denotes our final choice: PC1 to PC5, when we reach 82% accuracy. The baseline is to predict all ridge segments to be in the Atlantic basin, which has the most data. c) Feature importance is calculated from the decrease in classification accuracy by permuting data in each PC. Black bars show the standard deviation among all trees.

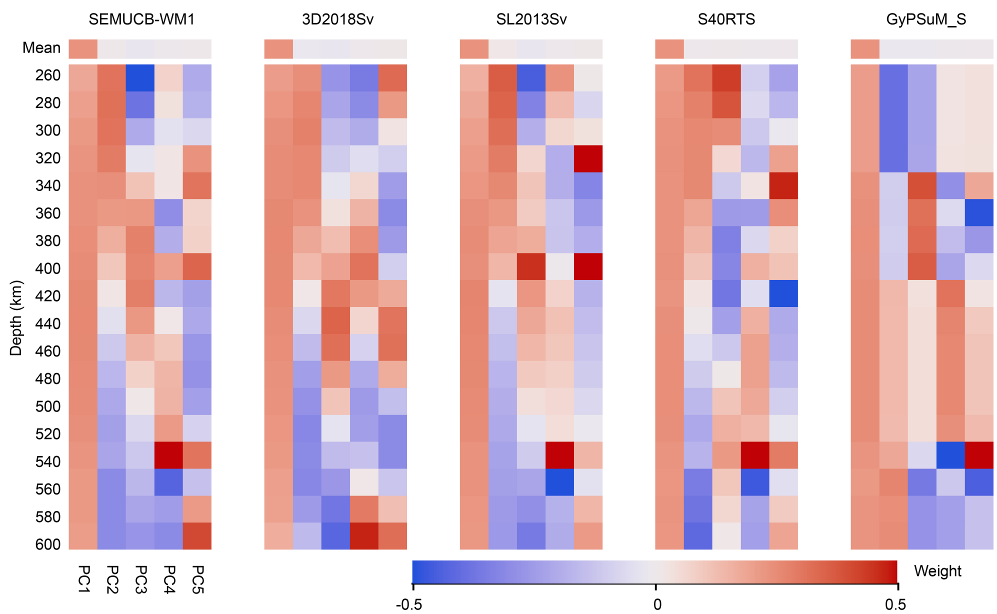

Figure 7: The PCA weight matrix of potential temperature at depth inferred from all tomographic models considered in this study.

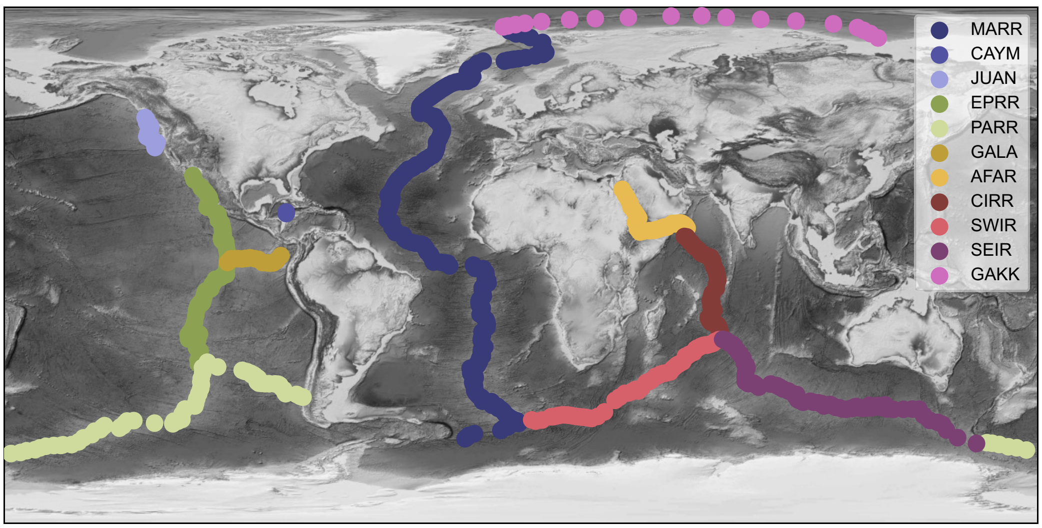

Figure 8: Sub-basin ridge systems as classified by our model. MARR: Mid-Atlantic Rise Ridge. CAYM: Cayman Ridge. JUAN: Juan De Fuca Ridge. EPRR: East Pacific Rise Ridge. PARR: Pacific-Antarctic Rise Ridge. GALA: Galapagos Ridge. AFAR: Red Sea Rift. CIRR: Central Indian Rise Ridge. SWIR: Southwest Indian Ridge. SEIR: Southeast Indian Ridge. GAKK: Gakkel Ridge.

Table 1: The confusion matrix from our classification models.

		Predicted			
		Atlantic	Indian	Pacific	Σ_{samples} [b]
Actual	Atlantic	88.0%[a]	6.8%	5.1%	2650
	Indian	8.7%	79.6%	11.7%	2050
	Pacific	10.5%	14.3%	75.1%	1850
	Σ_{samples} [b]	2707	2078	1765	6550

[a]Each row with percentages shows the fraction of all segments actually from a basin predicted to be in a different basin.
The diagonal parts are the correct predicted fractions.
[b]The last row and last column show the numbers of bootstrapped test samples summed over all 50 trained random forest models.

References

Ball, P.W., White, N.J., Maclennan, J., Stephenson, S.N., 2021. Global influence of mantle temperature and plate thickness on intraplate volcanism. Nature Communications 12, 1–13. doi:10.1038/s41467-021-22323-9.

Bao, X., Lithgow-Bertelloni, C.R., Jackson, M.G., Romanowicz, B., 2022. On the relative temperatures of Earth's volcanic hotspots and mid-ocean ridges. Science 375, 57–61. doi:10.1126/science.abj8944.

Brandl, P.A., Regelous, M., Beier, C., Haase, K.M., 2013. High mantle temperatures following rifting caused by continental insulation. Nature Geoscience 6, 391–394. doi:10.1038/ngeo1758.

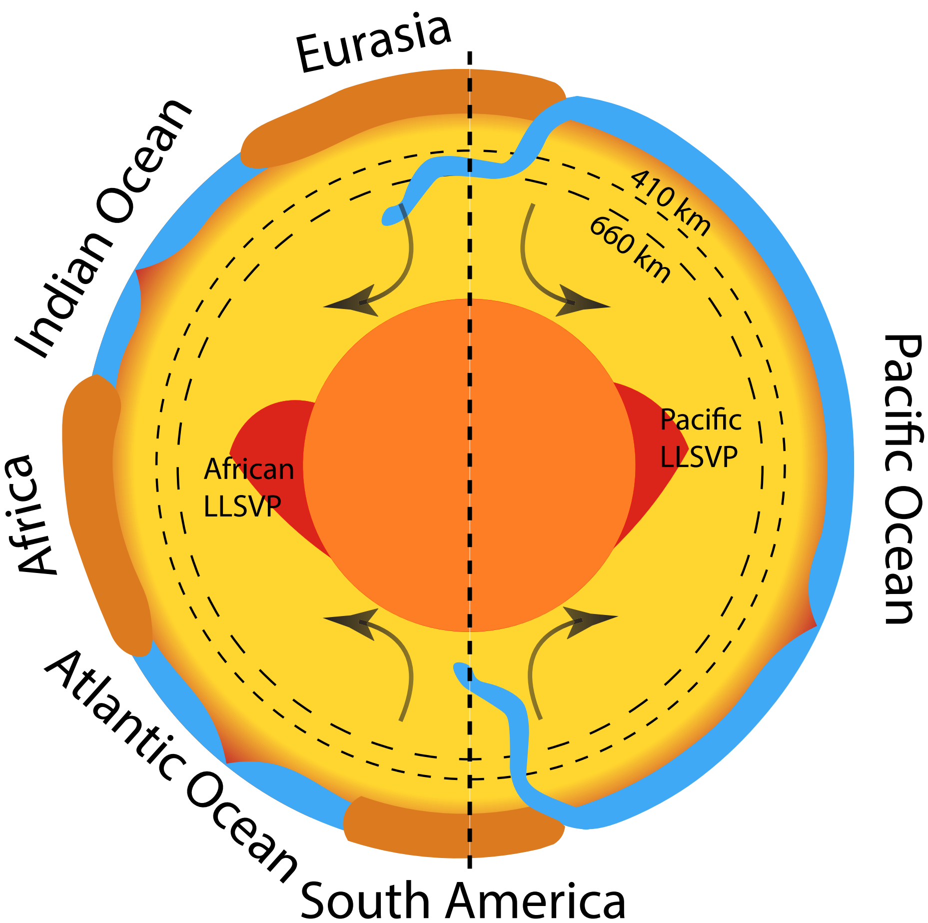

Figure 9: Schematic cross-section, showing how mantle convection and plate tectonics may affect present ridge temperature. Blue oceanic plates are subducted beneath brown continental plates, black arrows show the degree-2 convection pattern. The two red blobs are the LLSVPs. Note the hemispherical difference (degree-1, separated by the dashed line) from the lithosphere to the LLSVPs. Modified from Conrad and Ogliore, 2013.

Breiman, L., 2001. Random forests. Machine learning 45, 5–32.

Bridle, J., 1989. Training stochastic model recognition algorithms as networks can lead to maximum mutual information estimation of parameters. Advances in neural information processing systems 2.

Brown Krein, S., Molitor, Z.J., Grove, T.L., 2021. ReversePetrogen : A Multiphase Dry Reverse Fractional Crystallization-Mantle Melting Thermobarometer Applied to 13,589 Mid-Ocean Ridge Basalt Glasses. Journal of Geophysical Research: Solid Earth 126, 1–20. doi:10.1029/2020JB021292.

Conrad, C.P., Ogliore, T., 2013. URL: https://manoa.hawaii.edu/news/article.php?aId=5836.

Conrad, C.P., Steinberger, B., Torsvik, T.H., 2013. Stability of active mantle upwelling revealed by net characteristics of plate tectonics. Nature 498, 479–482. doi:10.1038/nature12203.

Dalton, C.A., Langmuir, C.H., Gale, A., 2014. Geophysical and Geochemical Evidence for Deep Temperature Variations Beneath Mid-Ocean Ridges. Science 344, 80–83. doi:10.1126/science.1249466.

Debayle, E., Bodin, T., Durand, S., Ricard, Y., Durand, S., 2020. Seismic evidence for partial melt below tectonic plates. Nature 586, 555–559. doi:10.1038/s41586-020-2809-4.

Debayle, E., Dubuffet, F., Durand, S., 2016. An automatically updated S-wave model of the upper mantle and the depth extent of azimuthal anisotropy. Geophysical Research Letters 43, 674–682. doi:10.1002/2015GL067329.

Demšar, J., Curk, T., Erjavec, A., Črt Gorup, Hočevar, T., Milutinovič, M., Možina, M., Polajnar, M., Toplak, M., Starič, A., Štajdohar, M., Umek, L., Žagar, L., Žbontar, J., Žitnik, M., Zupan, B., 2013. Orange: Data mining toolbox in python. Journal of Machine Learning Research 14, 2349–2353.

Duda, R.O., Hart, P.E., et al., 1973. Pattern classification and scene analysis. volume 3. Wiley New York.

French, S.W., Romanowicz, B.A., 2014. Whole-mantle radially anisotropic shear velocity structure from spectral-element waveform tomography. Geophysical Journal International 199, 1303–1327. doi:10.1093/gji/ggu334.

Gale, A., Langmuir, C.H., Dalton, C.A., 2014. The Global Systematics of Ocean Ridge Basalts and their Origin. Journal of Petrology 55, 1051–1082. doi:10.1093/petrology/egu017.

Gassmöller, R., Dannberg, J., Bredow, E., Steinberger, B., Torsvik, T.H., 2016. Major influence of plume-ridge interaction, lithosphere thickness variations, and global mantle flow on hotspot volcanism—the example of tristan. Geochemistry, Geophysics, Geosystems 17, 1454–1479. doi:10.1002/2015GC006177.

Gibson, S.A., Richards, M.A., 2018. Delivery of deep-sourced, volatile-rich plume material to the global ridge system. Earth and Planetary Science Letters 499, 205–218. doi:10.1016/j.epsl.2018.07.028.

Gurnis, M., 1988. Large-scale mantle convection and the aggregation and dispersal of supercontinents. Nature 332, 695–699. URL: https://www.nature.com/articles/332695a0, doi:10.1038/332695a0.

Gurnis, M., Müller, R.D., Moresi, L., 1998. Cretaceous Vertical Motion of Australia and the AustralianAntarctic Discordance. Science 279, 1499–1504. doi:10.1126/science.279.5356.1499.

Jellinek, A.M., Lenardic, A., 2009. Effects of spatially varying roof cooling on thermal convection at high Rayleigh number in a fluid with a strongly temperature-dependent viscosity. Journal of Fluid Mechanics 629, 109–137. doi:10.1017/S0022112009006260.

Jolliffe, I.T., 2002. Principal component analysis for special types of data. Springer.

Karlsen, K.S., Conrad, C.P., Domeier, M., Trønnes, R.G., 2021. Spatiotemporal Variations in Surface Heat Loss Imply a Heterogeneous Mantle Cooling History. Geophysical Research Letters 48, 1–10. doi:10.1029/2020GL092119.

Keller, T., Katz, R.F., Hirschmann, M.M., 2017. Volatiles beneath mid-ocean ridges: Deep melting, channelised transport, focusing, and metasomatism. Earth and Planetary Science Letters 464, 55–68. doi:10.1016/j.epsl.2017.02.006, arXiv:1608.03841.

Kimura, J.I., Sano, S., 2012. Reactive melt flow as the origin of residual mantle lithologies and basalt chemistries in mid-ocean ridges: Implications from the red hills peridotite, New Zealand. Journal of Petrology 53, 1637–1671. doi:10.1093/petrology/egs028.

Klein, E.M., Langmuir, C.H., 1987. Global correlations of ocean ridge basalt chemistry with axial depth and crustal thickness. Journal of Geophysical Research 92, 8089–8115. doi:10.1029/JB092iB08p08089.

Lenardic, A., Moresi, L., Jellinek, A.M., O'Neill, C.J., Cooper, C.M., Lee, C.T., 2011. Continents, supercontinents, mantle thermal mixing, and mantle thermal isolation: Theory, numerical simulations, and laboratory experiments. Geochemistry, Geophysics, Geosystems 12, 1–23. doi:10.1029/2011GC003663.

Meschede, M., Romanowicz, B., 2015. Lateral heterogeneity scales in regional and global upper mantle shear velocity models. Geophysical Journal International 200, 1078–1095. doi:10.1093/gji/ggu424.

Müller, R.D., Qin, X., Sandwell, D.T., Dutkiewicz, A., Williams, S.E., Flament, N., Maus, S., Seton, M., 2016. The gplates portal: Cloud-based interactive 3d visualization of global geophysical and geological data in a web browser. PloS one 11, e0150883. doi:10.1371/journal.pone.0150883.

Müller, R.D., Zahirovic, S., Williams, S.E., Cannon, J., Seton, M., Bower, D.J., Tetley, M.G., Heine, C., Le Breton, E., Liu, S., et al., 2019. A global plate model including lithospheric deformation along major rifts and orogens since the triassic. Tectonics 38, 1884–1907. doi:10.1029/2018TC005462.

Niu, Y., 2016. The Meaning of Global Ocean Ridge Basalt Major Element Compositions. Journal of Petrology 57, 2081–2103. doi:10.1093/petrology/egw073.

Niu, Y., O'Hara, M.J., 2008. Global correlations of ocean ridge basalt chemistry with axial depth: A new perspective. Journal of Petrology 49, 633–664. doi:10.1093/petrology/egm051.

O'Neill, C., Lenardic, A., Jellinek, A.M., Moresi, L., 2009. Influence of supercontinents on deep mantle flow. Gondwana Research 15, 276–287. doi:10.1016/j.gr.2008.11.005.

Ray, T.W., Anderson, D.L., 1994. Spherical disharmonies in the Earth sciences and the spatial solution: Ridges, hotspots, slabs, geochemistry and tomography correlations. Journal of Geophysical Research: Solid Earth 99, 9605–9614. doi:10.1029/94JB00340.

Ribe, N., Christensen, U., Theissing, J., 1995. The dynamics of plume-ridge interaction, 1: Ridge-centered plumes. Earth and Planetary Science Letters 134, 155–168. doi:10.1016/0012-821X(95)00116-T.

Ritsema, J., Deuss, A., Van Heijst, H.J., Woodhouse, J.H., 2011. S40RTS: A degree-40 shear-velocity model for the mantle from new Rayleigh wave dispersion, teleseismic traveltime and normal-mode splitting function measurements. Geophysical Journal International 184, 1223–1236. doi:10.1111/j.1365-246X.2010.04884.x.

Rodriguez, J., Kuncheva, L., Alonso, C., 2006. Rotation forest: A new classifier ensemble method. IEEE Transactions on Pattern Analysis and Machine Intelligence 28, 1619–1630. doi:10.1109/TPAMI.2006.211.

Rowley, D.B., Forte, A.M., Rowan, C.J., Glišović, P., Moucha, R., Grand, S.P., Simmons, N.A., 2016. Kinematics and dynamics of the East Pacific Rise linked to a stable, deep-mantle upwelling. Science Advances 2, e1601107. doi:10.1126/sciadv.1601107.

Schaeffer, A.J., Lebedev, S., 2013. Global shear speed structure of the upper mantle and transition zone. Geophysical Journal International 194, 417–449. doi:10.1093/gji/ggt095.

Simmons, N., Myers, S., Johannesson, G., Matzel, E., Grand, S., 2015. Evidence for long-lived subduction of an ancient tectonic plate beneath the southern indian ocean. Geophysical Research Letters 42, 9270–9278. doi:10.1002/2015GL066237.

Simmons, N.A., Forte, A.M., Boschi, L., Grand, S.P., 2010. GyPSuM: A joint tomographic model of mantle density and seismic wave speeds. Journal of Geophysical Research: Solid Earth 115. doi:10.1029/2010JB007631.

Sleep, N.H., 2002. Ridge-crossing mantle plumes and gaps in tracks. Geochemistry, Geophysics, Geosystems 3, 1–33. doi:10.1029/2001GC000290.

Spiegelman, M., Kelemen, P.B., 2003. Extreme chemical variability as a consequence of channelized melt transport. Geochemistry, Geophysics, Geosystems 4. doi:10.1029/2002GC000336.

Stewart, A.J., Li, Y., Cao, Z., Liu, L., 2023. Hemispheric dichotomy of mantle dynamics revealed by machine learning. arXiv preprint arXiv:2306.14312 .

Stixrude, L., Lithgow-Bertelloni, C., 2005. Thermodynamics of mantle minerals - I. Physical properties. Geophysical Journal International 162, 610–632. doi:10.1111/j.1365-246X.2005.02642.x.

Stixrude, L., Lithgow-Bertelloni, C., 2011. Thermodynamics of mantle minerals - II. Phase equilibria. Geophysical Journal International 184, 1180–1213. doi:10.1111/j.1365-246X.2010.04890.x.

Stracke, A., 2021. A process-oriented approach to mantle geochemistry. Chemical Geology 579, 120350.

Stracke, A., Willig, M., Genske, F., Béguelin, P., Todd, E., 2022. Chemical geodynamics insights from a machine learning approach. Geochemistry, Geophysics, Geosystems 23, e2022GC010606.

Torsvik, T.H., Burke, K., Steinberger, B., Webb, S.J., Ashwal, L.D., 2010. Diamonds sampled by plumes from the core-mantle boundary. Nature 466, 352–355. doi:10.1038/nature09216.

Workman, R.K., Hart, S.R., 2005. Major and trace element composition of the depleted MORB mantle (DMM). Earth and Planetary Science Letters 231, 53–72. doi:10.1016/j.epsl.2004.12.005.